Soft Matter

PAPER

View Article Online
View Journal | View Issue

Cite this: *Soft Matter*, 2025, **21**, 3012

Electric field-induced control of protein crystal morphology

Debes Ray, [ac] Mahnoush Madani, [b] Jan K.G. Dhont, [ab] Florian Platten *[ab] and Kyongok Kang *[a]

Received 19th February 2025,
Accepted 21st March 2025

DOI: 10.1039/d5sm00181a

rsc.li/soft-matter-journal

In a previous study (D. Ray, *et al.*, *J. Phys. Chem. Lett.*, 2024, **15**, 8108–8113), we found that an alternating electric field considerably affects the location of the crystallization boundary and the liquid–liquid phase separation line as well as crystallization kinetics in lysozyme solutions containing sodium thiocyanate (NaSCN). The present study extends this work by investigating the influence of the same electric field on the microscopic appearance of lysozyme crystals as they form from a supersaturated solution. We observe a variety of distinct crystal morphologies, which we classify as single- and multi-arm crystals, flower-like crystal structures, whiskers, and sea-urchin crystals. Crystal morphologies exhibit significant variations with changes in protein and salt concentrations, and the electric field strongly alters the morphology-state diagram in the protein-versus-salt concentration plane. This alteration is likely due to the field effect on protein–protein interactions. We believe the effect is mediated by the field-enhanced adsorption of SCN^- ions to the surface of lysozyme, ultimately driving the observed changes in crystallization behavior. These findings offer insights into how electric fields can be used to control crystal formation and morphology in protein systems.

1 Introduction

Protein solutions exhibit a variety of phase transitions,[1–6] including crystallization,[7–10] liquid–liquid phase separation (LLPS),[11–15] fibril formation,[16,17] gelation,[18,19] and cluster formation.[20] Protein crystallization, in particular, has attracted significant attention due to its role in structural biology, where the precise arrangement of protein molecules is essential for X-ray crystallography. The process of LLPS, although important in cellular processes, can sometimes compete with crystallization, as seen in studies on protein–salt mixtures like lysozyme and NaCl. The propensity of proteins to undergo these transitions is strongly influenced by their interactions with ions and other solution components.

Protein–protein interactions can be tuned by factors such as pH, salt type, salt concentration, and solution additives or precipitants, like PEG and cosolvents.[13,14,21–29] Interactions that are specific for proteins, which generally do not play a role for colloids, are due to specific binding of ions to the protein surface. This ion binding can alter the protein charge and lead to the formation of protein–ion–protein bridges[30–34] that influence protein aggregation and phase behavior. For example, thiocyanate ions (SCN^-) are known to bind more strongly to lysozyme than chloride ions (Cl^-), reducing the concentration of NaSCN required to induce crystallization or phase separation compared to NaCl.[35,36] The effect of NaCl on protein interactions is often explained by its ability to reduce the range of electrostatic repulsion with increasing salt concentration, which can promote both crystallization and LLPS.[27,37–40] In contrast, specific binding of certain multivalent ions can reverse the protein surface charge, leading to re-entrant LLPS.[21,32,41,42] Understanding these interactions is crucial not only for fundamental biological processes[43,44] but also for their applications in pharmaceuticals, food engineering, and the design of protein-based materials.[45–47] Furthermore, insights into these interactions could be applied to tune condensation pathways, with potential implications for other protein aggregation phenomena, such as fibrillation and amorphous aggregation.

One way to influence these interactions and modulate phase behavior is through external factors, such as electric fields. Specifically, direct current (DC) fields,[48] alternating current (AC) fields,[49–52] and pulsed fields[53] can affect key aspects of protein crystallization, such as crystal size, number, and diffraction quality.[54,55] The mechanisms underlying these effects include: (i) DC fields increasing protein and ion concentrations near electrodes, especially at sharp tips;[56,57] (ii) AC fields altering the chemical potentials of proteins in both liquid and crystalline phases;[58] and (iii) electric fields orienting

[a] *Institute of Biological Information Processing IBI-4, Forschungszentrum Jülich, 52428 Jülich, Germany. E-mail: k.kang@fz-juelich.de*
[b] *Faculty of Mathematics and Natural Sciences, Heinrich Heine University Düsseldorf, 40225 Düsseldorf, Germany. E-mail: florian.platten@hhu.de*
[c] *Solid State Physics Division, Bhabha Atomic Research Centre, Trombay, Mumbai 400085, India*

proteins and crystals.[59] However, these studies typically involve high field amplitudes (kV mm^{-1}), high frequencies (MHz), and ill-defined non-uniform field distributions, which complicate the interpretation and reproducibility of results.

In a previous study,[60] we investigated the effects of a weak AC electric field on lysozyme-NaSCN solutions using a well-defined geometry with two parallel flat electrodes. We observed a significant field-induced widening of the crystallization region: the crystallization boundary shifted to lower NaSCN concentrations, while the LLPS line moved to higher salt concentrations. A similar shift in the LLPS boundary was reported in ref. 61. The current study extends this work by exploring how the same electric field influences microscopic crystal morphology across different regions of the state diagram. In our earlier publication,[60] we proposed a possible mechanism for the observed widening of the crystallization region and the field-enhanced nucleation and growth. Here, we analyze possible effects of the electric field on the underlying interactions in greater detail, and conclude that field-induced ion binding provides a plausible mechanism for the observed effects.

This paper is organized as follows. The lysozyme-NaSCN system and the experimental setup are introduced, along with a brief discussion of the electric field strength experienced by proteins in bulk solution, which is screened by electrode polarization. The results section begins with the presentation of the morphology diagrams, both in the presence and absence of the electric field, followed by a description of the field-induced changes in the crystallization process, which lead to sharp transitions between different morphologies as a function of salt concentration. Next, possible mechanisms by which the electric field affects protein–protein interactions are discussed, proposing that the field enhances the binding of SCN^- ions to lysozyme. We further suggest how these changes in protein interactions may lead to the observed alterations in crystal morphology. These mechanisms are still tentative and require further investigation. The paper concludes with a summary of the findings and their implications.

2 Experimental methods

2.1 Sample preparation

Lysozyme is used as a model protein, dissolved in acetate buffer (pH 4.5) with sodium thiocyanate (NaSCN). At this pH, lysozyme carries a net charge of approximately + 11e, where e is the elementary charge. NaSCN is a more effective crystallization agent and precipitant than NaCl due to the stronger binding of SCN^- ions to the protein surface. NaSCN is expected to induce the formation of monoclinic lysozyme crystals.[35,36]

The sample solutions are prepared as described below (see ref. 60 and 62 for further details). Lysozyme (from chicken egg white powder, CAS No. 12650-88-3, Product No. 62971) and sodium thiocyanate (NaSCN, CAS No. 540-72-7, Product No. S7757) were purchased from Sigma-Aldrich. Lysozyme powder was dissolved in 50 mM sodium acetate buffer, pH 4.5, and filtered at least three times through a low-protein binding filter (Pall Corporation, Acrodisc Syringe Filters with 0.1 μm Supor membrane) to remove undissolved proteins or aggregates. NaSCN was also dissolved in the same buffer. The final concentrations of NaSCN and lysozyme stock solutions were determined using a combined density/refractive index measuring system (Anton Paar DMA 4500/RXA 156). Solutions (typically 100 μL) were prepared by mixing appropriate amounts of protein, salt, and buffer, then transferred to the microscopy sample cell, maintained at (24 ± 1) °C. At least three independently prepared samples were examined for each composition.

2.2 Experimental set-up

AC electric fields are applied using a Siglent SDG830 function generator. The custom-built electric sample cell has optically transparent indium–tin oxide (ITO)-coated glass electrodes, with a small electrode gap of L = 160 μm to minimize field-induced heating. Before use, the glasses are thoroughly rinsed with a water–ethanol mixture to remove any organic residues. We did not observe any degradation of the electrodes. The peak-to-peak voltage is fixed at V_{pp} = 1.0 V, and the angular frequency is $\omega = 2\pi/T = 2\pi f$, where T is the period of the AC field and f = 1 kHz is its frequency. For this electric field condition, we have observed significant effects on the phase boundaries,[60] and it is similar to those that have been shown to induce a response in amorphous protein aggregates.[63] The microscopic appearance of the crystals is monitored using an inverted polarized-light microscope (Zeiss Axiovert 40CFL) with an AxioCam Color CCD camera.

Due to electrode polarization, the electric field amplitude within the bulk of the protein solution, E_{bulk}, is lower than the externally applied field strength, $E_0 = V_{pp}/(2L)$,† as the electric double layers at the electrodes partially screen the charge that is externally applied to the electrodes (see ref. 64 and 65 and references therein):

$$E_{bulk} = \frac{\Omega}{\sqrt{4+\Omega^2}} E_0, \quad (1)$$

where the dimensionless number Ω is equal to,

$$\Omega = \frac{\omega L}{D\kappa}, \quad (2)$$

with $\kappa^{-1} = 0.304\,\mathrm{nm}/\sqrt{c_s/\mathrm{M}}$ being the Debye screening length (c_s is the salt concentration), and D is a typical value of the collective diffusion coefficient of the salt ions. For NaSCN, D = (1.5 ± 0.1) × 10^{-9} m^2 s^{-1}.[66,67] For example, at a typical salt concentration of c_s = 0.1 M, $\Omega \approx 1$. Converting the applied peak-to-peak voltage V_{pp} to the electric field amplitude E_{bulk} experienced by the proteins is essential for comparing the present data with experiments at different field strengths, frequencies, salt concentrations, and electrode gap widths.

† In our previous work,[60] we used $E_0 = V_{pp}/L$.

3 Results and discussion

3.1 Morphology diagrams

We observed different crystal morphologies, depending on the location within the state diagrams, specifically on protein and salt concentrations and the application of the electric field. The morphologies occur throughout the solution, not just in the vicinity of the electrodes. Fig. 1 shows the morphology-state diagram in the lysozyme *vs.* salt concentration plane, with (a) depicting the system without and (b) with the electric field. The various morphologies are marked by different symbols. The indicated points refer to the final crystal state, often reached after 24 hours, when no further microscopic changes are observed. This is a common timescale for the cessation of growth, but it may take months for equilibrium to be fully reached in the bulk,[68] likely due to slow long-term processes such as ripening or maturation. The solid lines represent the crystallization boundary and the LLPS state line, taken from ref. 60. In the present work, we differentiate between the various microscopic crystal morphologies, which were previously considered simply as crystals. The region between these two lines is referred to as the "crystal region" or "crystallization gap" in some literature.[10] Crystallization, however, also occurs above the metastable LLPS line, where a rapid increase in turbidity is observed due to LLPS, but the final stable state remains crystalline.

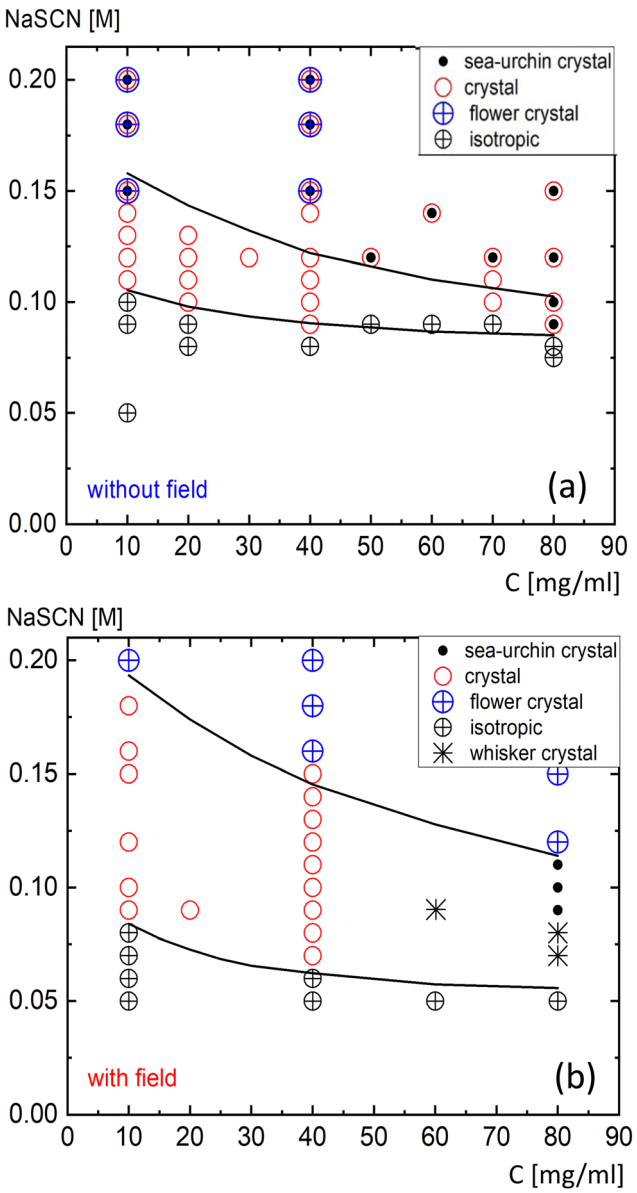

Fig. 1 The morphology-state diagram (a) in the absence and (b) in the presence of the external electric field. The observed crystal morphologies are labelled in the right top corners, with further definitions provided in Fig. 2. The applied field strength is E_0 = 3 V mm^{-1} with a frequency of f = 1 kHz. As a guide to the eye, the solid lines represent the crystallization boundary (lower line) and the LLPS phase boundary (upper line).

The various crystal morphologies distinguished in this study are depicted in Fig. 2. The symbols used to represent these morphologies in Fig. 1 are shown in the upper right corner of the microscopy images in Fig. 2. These include single crystals, crystals with a few arms originating from a common nucleus (or nearby nuclei), and crystals with many arms, as shown in Fig. 2a–c, all represented by a single symbol (a red circle). We consistently observe a mixture of these three morphologies, with a wide variation in their sizes. These will hereafter be referred to simply as "crystals". The relative abundance of these structures depends on the location in the state diagram, as discussed below. We also observe compact crystal assemblies with similar arm dimensions, forming a sharp periphery, which we refer to as "flower-like crystals" (Fig. 2d). Needle-like crystals with a preferred orientation, as shown in Fig. 2e, which we refer to as "whiskers", are only found in the presence of the electric field, at high protein concentration and low salt concentration within the crystal region (see the lower right region in Fig. 1b). An example is shown in Fig. 2e. Lastly, spherulitic "sea-urchin

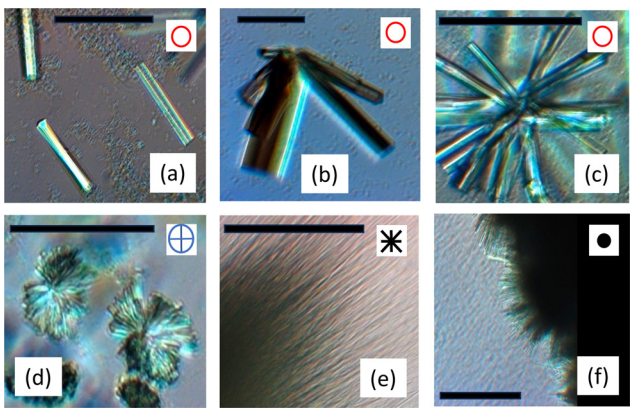

Fig. 2 Microscope images of various crystal morphologies: (a) single crystals, (b) conic crystals with a few arms, (c) multi-arm crystals, (d) flower-like crystals, (e) whiskers, and (f) sea-urchin crystals. The scale bars indicate 200 μm. The symbols representing these morphologies in Fig. 1 are shown in the upper right corner of each image. A mixture of the three morphologies (a)–(c) is consistently observed, with a wide variation in size. These are referred to as "crystals" in the text and are represented by the same symbol. The regions where different crystal forms predominantly occur are highlighted in Fig. 3.

crystals'' are observed (Fig. 2f). These are more compact than whiskers, with single crystals emerging from the periphery. Sea-urchin crystals are often considered undesirable for crystallographic studies,[69] but, as will be discussed below the formation of this species is largely suppressed by the application of an electric field. Sea-urchin crystals have been reported previously, such as in ref. 14, 40 and 70–72, where NaCl was used as the precipitant, although these structures are sometimes less compact. In the present work, using NaSCN as the precipitant and the protein concentrations investigated, we do not observe a gel phase like in ref. 14, 19 and 37. The homogeneous, isotropic state, where no crystals are formed, is indicated in the morphology-state diagrams by black encircled crosses. The morphologies (a)–(d) likely represent the monoclinic polymorph, as expected in the presence of NaSCN.[35,36] For morphologies (e) and (f), this is not clear, and a sufficient amount of material would be required for diffraction studies to enable unambiguous crystallographic identification. For the sea-urchin morphology (f), it has already been shown that it does not correspond to the standard tetragonal form.[70]

The morphology diagram in Fig. 3 is similar to that in Fig. 1, but now includes a differentiation between the regions where specific crystal forms, as shown in Fig. 2a–c, occur in majority. Representative images are provided in the left panel. Single crystals dominate near the lower crystallization boundary (indicated by the green square, up to the green broken line). For protein concentrations below approximately 50 mg mL^{-1}, crystals with a few arms and a conic shape are found upon increasing salt concentration (indicated by the blue square). As salt concentration increases further, the number of arms increases (orange square). The number of arms also increases with protein concentration at a fixed salt level (middle image, left panel). At even higher salt or protein concentrations, crystals with nearly fully packed arms, resembling flower-like crystals, are formed (red square). The dotted black line in Fig. 3 marks the region where only whiskers and sea urchins are observed. Since the relative abundance of different crystal morphologies changes gradually, the broken and dotted lines are approximate and serve as guides to the eye.

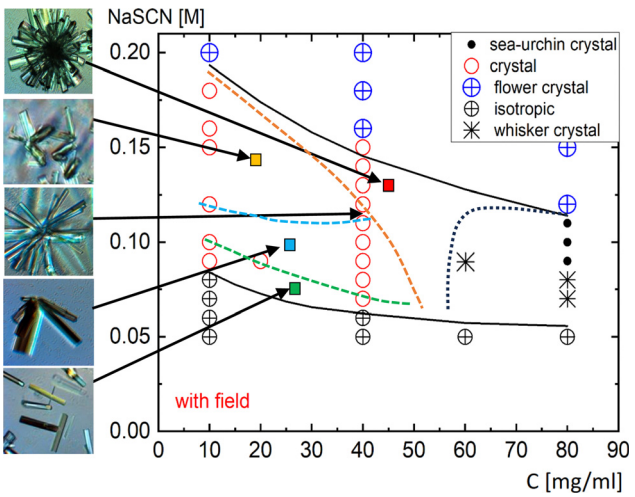

Fig. 3 The same morphology diagram as in Fig. 1b, in the presence of an electric field (E_0 = 3 V mm^{-1}, f = 1 kHz) now showing the regions where different crystal forms predominantly occur. The left panel images represent typical crystal forms (the lower three correspond to those in Fig. 2a–c). The green square indicates the region of single crystals, the blue square corresponds to conic crystals with a few arms, the orange square denotes crystals with more arms than the conic crystals, and the red square represents crystals with almost fully packed arms. The dashed lines outline the regions where these crystal types are found, and the black dotted line marks the region where only whiskers and sea-urchin crystals are observed.

There are notable differences between the morphology diagrams for NaSCN and NaCl as precipitants. The morphology diagram for NaCl, in the absence of an electric field, has been previously reported (*e.g.*, in ref. 71). At high salt concentrations, single (tetragonal) crystals are found, with sea-urchin crystals appearing at even higher concentrations. In contrast to the NaSCN system (Fig. 1a), where sea-urchin crystals always coexist with other crystal forms, sea-urchin crystals in the NaCl system seem to appear independently at high salt and protein concentrations, without the simultaneous presence of crystals, contrary to what is seen in Fig. 1a, where sea-urchins always occur in combination with crystals. However, it is possible that this behavior could also occur at higher NaSCN concentrations than those studied here, where we intentionally limited our investigation to lower concentrations in order to avoid field-induced heating. In contrast, investigating the influence of electric fields on lysozyme-NaCl solutions would not be practical, as the elevated salt concentration would likely cause field-induced heating, which could significantly distort the observed effects, especially given their temperature sensitivity.

3.2 Effect of the electric field on morphology transitions

Fig. 4 and 5 illustrate the sharp transitions in crystal morphologies as a function of salt concentration, under the influence of an electric field. The images, arranged from left to right, show the crystallization process at three stages: early, intermediate, and final. At a lower protein concentration of 40 mg mL^{-1} (Fig. 4), crystals dominate throughout the crystallization region below the LLPS line (Fig. 4a, with the electric field applied). As the salt concentration increases, small flower-like crystals form above the LLPS line (Fig. 4b). High turbidity, indicative of low transparency, is evident in the dark brown appearance in Fig. 4b and c, resulting from long-wavelength concentration inhomogeneities during the early stages of liquid–liquid demixing, as previously observed in lysozyme solutions.[73] In the final stage, in the absence of the electric field, a dense mixture of crystals, flower-like crystals, and sea urchins is observed above the LLPS line (Fig. 4c). The salt concentration and field dependencies of crystal morphologies at 40 mg mL^{-1} are characteristic of low protein concentrations.

In contrast, at the higher protein concentration of 80 mg mL^{-1} (Fig. 5), the crystallization process exhibits different morphology transitions. Below the LLPS line (Fig. 5a), only sea-urchin crystals form, while above the LLPS line (Fig. 5b), small crystals initially appear, from which larger flower-like crystals grow at the expense of the smaller ones. Compared to

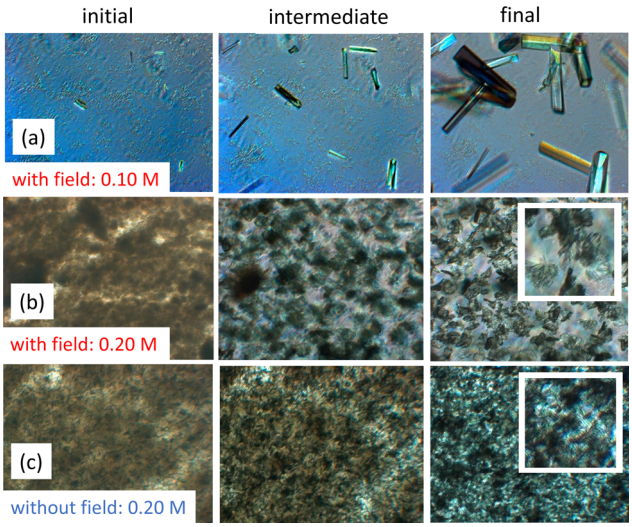

Fig. 4 Protein crystallization under electric field conditions at a concentration of 40 mg mL^{-1}, illustrating sharp transitions in crystal morphologies with varying salt levels at low protein concentrations. From left to right: images in the initial, intermediate, and final stages of crystallization. Field of view: 600 × 500 μm^2. (a) With the electric field (E_0 = 3 V mm^{-1}, f = 1 kHz), for a NaSCN concentration of 0.10 M, below the LLPS line. (b) As in (a), but for 0.20 M, above the LLPS line. (c) Without the electric field, for 0.20 M, above the LLPS line. The inserts in (b) and (c) show a field of view of 150 × 150 μm^2.

the flower-like crystals formed at 40 mg mL^{-1} (Fig. 4), those at 80 mg mL^{-1} are significantly larger. The effect of the electric field is highlighted when comparing the images in Fig. 5b and c, both of which are above the LLPS line. Without the electric

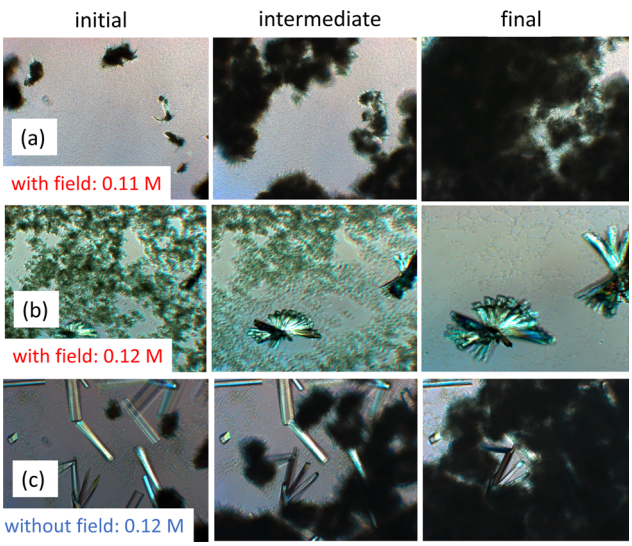

Fig. 5 Protein crystallization under electric field conditions at a protein concentration of 80 mg mL^{-1}, illustrating sharp transitions in crystal morphologies with varying salt levels at high protein concentrations. From left to right: images in the initial, intermediate, and final stages of crystallization. Field of view: 600 × 500 μm^2. (a) With the electric field (E_0 = 3 V mm^{-1}, f = 1 kHz), for a NaSCN concentration of 0.11 M, slightly below the LLPS line. (b) As in (a), but for 0.12 M, slightly above the LLPS line. (c) Without the electric field, for 0.12 M, slightly above the LLPS line.

field (Fig. 5c), both crystals and sea urchins coexist. In contrast, in the presence of the electric field (Fig. 5b), only flower-like crystals are observed. The reason that turbid images due to LLPS appear at 40 mg mL^{-1} but not at 80 mg mL^{-1} is that at 80 mg mL^{-1}, LLPS occurs much more rapidly.

Within the crystal region of the morphology-state diagram (Fig. 1b) for 80 mg mL^{-1}, in the presence of the electric field, whiskers form at relatively low salt concentrations, and at higher salt concentrations, sea urchins are observed. In contrast, in the absence of the electric field (Fig. 1a), both crystals and sea urchins coexist in the crystal region.

The overall effect of the electric field above the LLPS line is that it not only widens the crystallization region, but also suppresses the formation of mixed states, where multiple crystal forms coexist. At low protein concentrations, mixed states observed without the electric field are replaced by the exclusive formation of flower-like crystals in the presence of the field. At high concentrations, mixed states, observed in the absence of the electric field (Fig. 1a), are also eliminated under field conditions (Fig. 1b), where only flower-like crystals form above the LLPS line. Furthermore, at 80 mg mL^{-1}, within the crystal region (between the crystallization boundary and the LLPS line), the electric field promotes the formation of either sea urchins or whiskers (Fig. 1b), whereas in its absence, a mixed state of crystals and sea urchins is observed (Fig. 1a).

Obviously, the sharp transition of crystal morphologies upon crossing the LLPS line is connected to phase separation (see, *e.g.*, ref. 74 for further details on phase separation). Simulations show that nucleation as well as crystal growth are enhanced just below the critical point due to long-lived regions or droplets with higher protein concentration.[75,76] This suggests fast nucleation and crystal growth above the LLPS line, either during the initial Cahn–Hilliard stage of liquid–liquid demixing, within the labyrinthine regions of higher protein concentration, or in droplets formed during the later stage of spinodal demixing, or in droplets nucleating between the liquid–liquid binodal and spinodal, or close to these droplets.

3.3 A scenario for the effect of electric fields on protein–protein interactions

An electric field can, in principle, influence protein–protein interactions. Such changes in interactions impact phase behavior and crystal morphology. Here, we discuss potential mechanisms through which an electric field could affect the pair-interaction potential.

As mentioned in our previous publication,[60] the effect of electric fields on phase behavior and crystallization kinetics can be attributed to an electric field-induced change of the interaction potential between the proteins. The overall, orientationally averaged interaction potential becomes less attractive under the electric field, while attractive interactions for specific protein orientations that promote crystallization are enhanced.

Several mechanisms could explain how an electric field affects protein–protein interactions. However, the effects discussed below are negligible for small proteins like lysozyme:

(i) The permanent electric dipole moment of lysozyme induces alignment in an electric field, enhancing overall attractions. However, due to the small dipole moment of lysozyme, these field-induced alignment effects are negligible (see Appendix). Much stronger electric fields are required for significant orientation.[59]

(ii) Polarization of the diffuse electric double layer increases overall attractions. However, for the field strength considered, and given the relatively small size of lysozyme, the induced dipole moments are insignificant (see Appendix).

(iii) Changes in the secondary or tertiary structure of lysozyme that could alter interactions would require much larger field strengths.[61,77–79]

(iv) The potential role of lysozyme-cluster formation, as discussed in ref. 41, 80 and 81, can likely be excluded for the salt concentrations considered, as the observed state diagram (Fig. 1) represents a system dominated by short-range attractions, where repulsions play only a minor role. However, it is conceivable that such effects could occur at even lower salt concentrations.

The mechanisms discussed in ref. 60 can thus be excluded.

The adsorption of thiocyanate ions to lysozyme and the ion bridges between proteins[82,83] are thought to be at the origin of lysozyme crystallization and LLPS. In view of the preceding discussion, it is therefore plausible that the effect of the electric field influences phase behavior by altering the adsorption of SCN^- ions. A field-induced increase in the number of adsorbed ions is expected to enhance protein–protein attractions, both by reducing the associated decrease of the net charge of the protein and by increasing the number of ion bridges between the proteins. This would explain the observed shift of the LLPS line to higher salt concentrations under the electric field (Fig. 1). Additionally, since more ions adsorb to the lysozyme molecules in the presence of the electric field, less salt is required to induce crystallization. Consequently, the crystallization boundary is expected to shift to lower salt concentrations, as observed in our experiments (Fig. 1).

Moreover, field-induced adsorption of ions may alter the anisotropic, orientation-dependent interactions between proteins. These changes could enhance protein–protein attractions for specific orientations, which might explain the observed increase in nucleation and crystal growth rates, as reported in ref. 60.

At higher pH, where the net charge is significantly smaller, cloud-point temperatures were observed to increase with NaSCN concentration at low NaSCN levels, but decrease above approximately 0.4 M (Fig. 2 in ref. 83). These changes in cloud point reflect alterations in protein–protein interactions,[28,62,84] with initial increases followed by decreases in net attractions as salt concentration rises. At a fixed temperature, this results in re-entrant LLPS, where above a certain NaSCN concentration (around 1.2 M at 20 °C, ref. 83), the solution becomes transparent and homogeneous again. However, we did not observe this behavior at the lower pH considered here (data not published).

The question arises why the electric field might increase the number of adsorbed SCN^- ions. The most likely explanation is

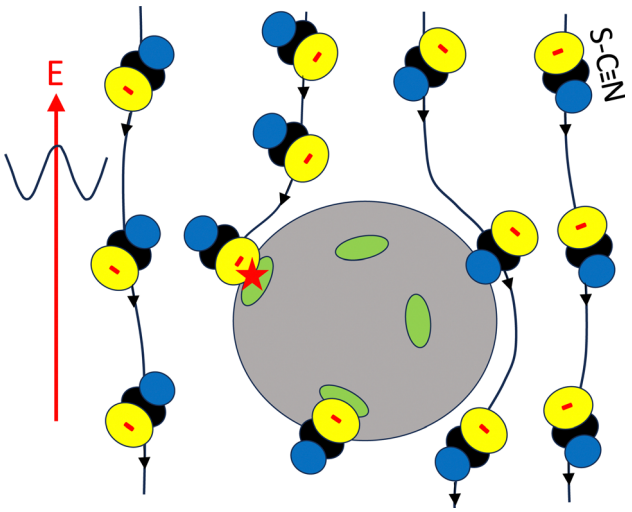

Fig. 6 A schematic of the proposed mechanism, where the electric field-induced transport of SCN^- ions towards the periphery of lysozyme molecules promotes additional ion binding. The grey body represents a lysozyme molecule, the green patches denote binding sites for the ions. The lines are the streamlines along which SCN^- ions are transported. The red star indicates the field-induced binding of an ion. The lower SCN^- ion is already bound in the absence of the electric field, while the remaining ions pass by the lysozyme molecule without binding. For clarity, only SCN^- ions are shown here.

that the electric field induces a flux of SCN^- ions toward the protein surface, thereby increasing the number of adsorbed ions (see Fig. 6, which illustrates this mechanism). This is analogous to the increased crystal growth rates observed for colloids under weak shear flow, where solvent flow transports colloidal particles towards crystal surfaces.[85,86] However, for stronger shear flow, the crystal growth rate is diminished, due to the removal of colloids from the crystal surface by strong hydrodynamic forces.[85] Similarly, for sufficiently strong electric fields, SCN^- ions might be removed from the lysozyme surface, which could reduce crystal growth rates. In ref. 87, the number of crystals formed with NaCl as a precipitant was measured as a function of electric field strength within a range similar to the one used in our study. There, the lowest field strength diminished the number of crystals formed, while higher field strengths increased their number. Furthermore, crystal size was inversely correlated with the number of crystals. This non-monotonic behavior is consistent with the proposed mechanism: low field strengths might enhance crystal growth, while high field strengths could hinder it.

To unambiguously validate the above assertions, neutron and X-ray scattering experiments, as well as single crystal X-ray diffraction (similar to those in ref. 30 for NaCl as a precipitant), should be conducted to resolve protein–protein interactions and the atomistic structure of single lysozyme molecules interacting with SCN^- ions in the presence of an electric field.

3.4 Potential mechanisms by which electric fields affect crystal morphologies

Predicting phase behavior from a known pair-interaction potential is complex and analytically challenging, especially

in this case. Atomistic simulations are needed to fully understand how electric fields influence interactions and phase behavior at the molecular level. As a result, the discussion of the physical mechanisms behind electric field effects on crystal morphology remains speculative at this point.

As outlined above, the electric field has two main effects on crystal formation. In its absence, mixed crystal forms coexist, with multiple morphologies present in the final stage. However, under the influence of the electric field, only a single crystal morphology is observed. Furthermore, at high protein concentrations below the LLPS line, the electric field induces the formation of whiskers, a morphology not seen in its absence.

The electric field eliminates the coexistence of multiple crystal forms, particularly above the LLPS line, where only flower-like crystals are observed. This suggests that the field promotes the formation of a single, specific crystal morphology. One possible explanation for this effect is that the electric field enhances the adsorption of SCN^- ions at specific sites on the lysozyme surface. This enhanced adsorption could induce an attractive pair-interaction potential for specific protein orientations, lowering the energy barrier for nucleation and/or crystal growth for one particular crystal morphology. This scenario would also explain the observed field-induced diminished induction times and enhanced crystal growth rates reported in ref. 60. While the resulting crystal forms are kinetically stable, the true thermodynamically stable morphology may take much longer to develop. Our observations show that these morphologies remain stable for several weeks.

The formation of long, thin crystals, such as whiskers, can be explained by the rapid nucleation and crystal growth conditions facilitated by the electric field. Fast nucleation results in disordered, transient nuclei that reorganize into a stable assembly of nuclei with varying orientations. These nuclei grow radially, leading to the formation of elongated, needle-like structures. The anisotropic growth, where the length of the crystal increases much faster than the other dimensions, is likely driven by the influence of the field on ion transport to nucleation sites and crystal surfaces. This alters protein–protein interactions, promoting rapid elongation along one axis. As a result, the growth is kinetically controlled, with the electric field favoring the formation of specific morphologies, such as whiskers.

We also speculate on the mechanisms behind the formation of sea-urchin, multi-arm, and flower-like crystals, as well as the influence of the electric field on nucleation. Sea-urchin crystals are closely tied to phase separation and the formation of localized regions of high supersaturation, which promote multiple nucleation events growing radially outward. Without the electric field, these crystals form naturally at higher protein concentrations, particularly above the LLPS line, due to the creation of multiple nucleation sites. However, when an electric field is applied, the electric field alters protein–protein interactions and nucleation kinetics, suppressing the formation of sea-urchin morphology above the LLPS line. Instead, the field favors the formation of more ordered, flower-like crystals, consistent with the influence of the field on protein orientation during nucleation.

Multi-arm crystals, as shown in Fig. 2b and c, also grow radially from a central region, but their arms are not needle-like. Below the LLPS line, and for protein concentrations below approximately 50 mg mL^{-1}, the number of arms seems to increase gradually as the protein and/or salt concentration rises, as discussed in connection to Fig. 3. This transition can be attributed to the effects of supersaturation, which accelerate nucleation. As supersaturation increases, nucleation events occur more frequently and in close proximity, resulting in multiple nucleation sites within a small region of the solution. These sites grow independently, and the arms form as each site competes for the available solute.

The flower-like crystals observed above the LLPS line appear to have the maximum geometrically possible number of arms. This phenomenon can be explained by the rapid phase separation above the LLPS line, which creates protein concentration inhomogeneities through nucleation or spinodal decomposition. These inhomogeneities lead to local regions of high supersaturation, promoting simultaneous nucleation events in close proximity. This results in multiple crystal growth sites emerging almost simultaneously, each growing outward from a central point, forming multiple arms, as observed in our experiments.

In addition, the electric field can accelerate nucleation and crystal growth by enhancing ion transport towards nucleation sites and crystal surfaces. This enhanced transport reduces the formation of certain aggregates, promoting more uniform nucleation of a single crystal morphology.

4 Conclusion

In summary, we have extended our previous work[60] on the effects of electric fields on state boundaries and crystallization kinetics, now examining microscopic crystal morphologies in greater detail. We observe a variety of crystal forms, including single crystals, multi-arm crystals, flower-like crystals as well as needle-like sea urchins and whiskers.

Without an electric field, single crystals and multi-arm crystals coexist below the LLPS line at lower protein concentrations. At higher protein concentrations, sea-urchin crystals form in addition to these two types. Above the LLPS line, where phase separation precedes crystallization, flower-like crystals emerge alongside the morphologies observed below the LLPS line. These flower-like crystals consist of closely packed multi-arm structures with similar arm dimensions.

On applying the electric field, the diversity of crystal morphologies is reduced, and only flower-like crystals are observed above the LLPS line, with no coexistence of different morphologies. At high protein concentrations, a new crystal morphology – whiskers – emerges, which does not form in the absence of the electric field. These whiskers consist of numerous long, thin needle-like structures that grow in a preferred direction.

We attribute these field-induced changes in crystal morphology to alterations in the protein–protein interaction potential,

likely driven by the field-enhanced transport of salt ions, particularly thiocyanate ions, to the protein surface. The field-induced adsorption reduces the total positive charge of the proteins, thereby decreasing their repulsive interactions. Furthermore, the increased number of salt bridges between proteins enhances attractive interactions. These effects explain both the shift of the LLPS line to higher salt concentrations and the shift of crystallization boundary to lower salt concentrations. In addition, we speculate on potential mechanisms underlying the observed crystal morphologies and the effect of the electric field. It would be very interesting to examine whether the suggested mechanisms could also explain future experiments, in which we plan to systematically investigate the dependence of the state diagram, crystal morphologies, and the associated formation kinetics on field strength and frequency. The different morphologies may correspond to distinct crystal structures, which could be investigated using cryo-TEM experiments.

Beyond crystal formation, these findings may have broader implications for understanding and guiding protein self-assembly processes, such as amorphous aggregation and fibril formation. Electric field-induced alterations in protein interactions, solution organization, and ion transport could influence self-assembly pathways in other protein systems. Further investigation of these effects may thus aid in the design of novel protein-based materials and enhance our understanding of pathological conditions associated with protein aggregation.

Data availability

The data that support the findings of this study are available within the article.

Conflicts of interest

There are no conflicts to declare.

Appendix

The alignment of proteins induced by an electric field can influence their mutual interactions. In the absence of an electric field, lysozyme has a dipole moment of $p_0 = 25e$ Å (with the elementary charge e), which corresponds to 122D.[88] Even if these dipoles were perfectly aligned along the external field, the resulting dipole–dipole interaction is still much smaller than the thermal energy k_BT (with k_B Boltzmann's constant and T the temperature). The pair-interaction potential V_p of two such parallel dipoles separated by a distance $\boldsymbol{R}$ is equal to,

$$V_p(\boldsymbol{R}) = \frac{{p_0}^2}{4\pi\varepsilon R^3}\left[1 - 3\cos^2(\Theta)\right], \tag{3}$$

where ε is the dielectric constant of water (in absolute units) and Θ is the angle between the electric field direction and the vector connecting the dipoles. Averaging the pair-interaction potential over the orientation of their distance vector $\boldsymbol{R}$ with respect to the Boltzmann probability to leading order in the external field strength leads to,

$$V_p(\boldsymbol{R}) = -\frac{4}{5}\frac{1}{k_BT}\left(\frac{{p_0}^2}{4\pi\varepsilon R^3}\right)^2. \tag{4}$$

Note that this interaction potential is negative, and thus leads to increased overall attractions, contrary to what is seen experimentally. However, for $R > 2a$, with $a = 1.7$ nm the radius of lysozyme, with $\varepsilon = 7 \times 10^{-10}$ C Vm^{-1}, and at 24 °C, where $k_BT = 4 \times 10^{-21}$ Nm, the interaction potential $V_p(R)/k_BT$ is found to be less than 10^{-2}. Therefore, these alignment-induced interactions are negligible.

Moreover, the field strengths experienced by the particles, E_{bulk}, is on the order of 1 V mm^{-1} and is therefore too small to induce significant alignment. The thermally averaged cosine of the angle Θ between the electric field and the dipole direction is given by,

$$\langle\cos\Theta\rangle = \frac{p_0}{3k_BT}E_{bulk} \tag{5}$$

where the brackets $\langle\cdot\rangle$ denote thermal averaging. Using the values mentioned above, we obtain $\langle\cos\Theta\rangle \sim 10^{-5}$, indicating that all orientations of a lysozyme molecule are essentially equally probable.

Electric dipoles can also arise from the deformation of the charge distribution within the solvent near the protein surface. Since the surface charge is small, typically a few elementary charges, which is equal to the total charge within the double layer, the polarization of the double layer at most gives rise to a dipole moment on the order of a few e Å. As discussed above, such dipoles are too weak to significantly affect protein–protein interactions. Additionally, there is a contribution to the total field-induced dipole moment, unrelated to the total charge within the double layer, known as volume polarization. This induced dipole, p_0^{vol}, results from ion accumulation as ions move past the protein's core. The maximum value of this dipole moment (at zero frequency) due to volume polarization is given by,[89,90]

$$p_0^{vol} = 2\pi\varepsilon a^3\frac{1 + \kappa a + \frac{2}{3}(\kappa a)^2}{1 + \kappa a + \frac{1}{3}(\kappa a)^2}E_{bulk} \tag{6}$$

with a direction opposite to the electric field. Hence, $p_0^{vol} \sim 10^{-2}\ e$ Å, corresponding to a very small fraction of an elementary charge on each side of the lysozyme molecule. As before, such dipole moments are insignificant.

Acknowledgements

Financial support by the German Research Foundation (DFG Grant No. 495795796) is gratefully acknowledged.

References

1 J. D. Gunton, A. Shiryayev and D. L. Pagan, *Protein condensation. Kinetic pathways to crystallization and disease*, Cambridge University Press, 2007.

2 A. Stradner and P. Schurtenberger, *Soft Matter*, 2020, **16**, 307–323.
3 A. C. Dumetz, A. M. Chockla, E. W. Kaler and A. M. Lenhoff, *Biophys. J.*, 2008, **94**, 570–583.
4 P. G. Vekilov, *Soft Matter*, 2010, **6**, 5254–5272.
5 R. Mezzenga and P. Fischer, *Rep. Prog. Phys.*, 2013, **76**, 046601.
6 J. J. McManus, P. Charbonneau, E. Zaccarelli and N. Asherie, *Curr. Opin. Colloid Interface Sci.*, 2016, **22**, 73–79.
7 C. R. Berland, G. M. Thurston, M. Kondo, M. L. Broide, J. Pande, O. Ogun and G. B. Benedek, *Proc. Nat. Acad. Sci. U. S. A.*, 1992, **89**, 1214–1218.
8 O. Galkin and P. G. Vekilov, *Proc. Nat. Acad. Sci. U. S. A.*, 2000, **97**, 6277–6281.
9 S. D. Durbin and G. Feher, *Annu. Rev. Phys. Chem.*, 1996, **47**, 171–204.
10 D. Fusco and P. Charbonneau, *Colloids Surf., B*, 2016, **137**, 22–31.
11 C. Ishimoto and T. Tanaka, *Phys. Rev. Lett.*, 1977, **39**, 474–477.
12 J. A. Thomson, P. Schurtenberger, G. M. Thurston and G. B. Benedek, *Proc. Nat. Acad. Sci. U. S. A.*, 1987, **84**, 7079–7083.
13 Y. Wang, A. Lomakin, R. F. Latypov, J. P. Laubach, T. Hideshima, P. G. Richardson, N. C. Munshi, K. C. Anderson and G. B. Benedek, *J. Chem. Phys.*, 2013, **139**, 121904.
14 M. Muschol and F. Rosenberger, *J. Chem. Phys.*, 1997, **107**, 1953–1962.
15 F. Platten, N. E. Valadez-Pérez, R. Castañeda Priego and S. U. Egelhaaf, *J. Chem. Phys.*, 2015, **142**, 174905.
16 T. C. T. Michaels, D. Qian, A. Saric, M. Vendruscolo, S. Linse and T. P. J. Knowles, *Nat. Rev. Phys.*, 2023, **5**, 379–397.
17 C. Brangwynne, P. Tompa and R. Pappu, *Nat. Phys.*, 2015, **11**, 899–904.
18 T. Gibaud, F. Cardinaux, J. Bergenholtz, A. Stradner and P. Schurtenberger, *Soft Matter*, 2011, **7**, 857–860.
19 J. Hansen, C. J. Moll, L. López Flores, R. Castañeda-Priego, M. Medina-Noyola, S. U. Egelhaaf and F. Platten, *J. Chem. Phys.*, 2023, **158**, 024904.
20 A. Stradner, G. M. Thurston and P. Schurtenberger, *J. Phys.: Condens. Matter*, 2005, **17**, S2805.
21 F. Zhang, F. Roosen-Runge, A. Sauter, M. Wolf, R. M. J. Jacobs and F. Schreiber, *Pure Appl. Chem.*, 2014, **86**, 191–202.
22 J. Hansen, F. Platten, D. Wagner and S. U. Egelhaaf, *Phys. Chem. Chem. Phys.*, 2016, **18**, 10270–10280.
23 S. N. Timasheff, *Proc. Nat. Acad. Sci. U. S. A.*, 2002, **99**, 9721–9726.
24 A. S. Parmar and M. Muschol, *Biophys. J.*, 2009, **97**, 590–598.
25 M. L. Broide, T. M. Tominc and M. D. Saxowsky, *Phys. Rev. E: Stat. Phys., Plasmas, Fluids, Relat. Interdiscip. Top.*, 1996, **53**, 6325–6335.
26 V. G. Taratuta, A. Holschbach, G. M. Thurston, D. Blankschtein and G. B. Benedek, *J. Phys. Chem.*, 1990, **94**, 2140–2144.
27 M. Muschol and F. Rosenberger, *J. Chem. Phys.*, 1995, **103**, 10424–10432.
28 F. Platten, J. Hansen, J. Milius, D. Wagner and S. U. Egelhaaf, *J. Phys. Chem. Lett.*, 2016, **7**, 4008–4014.
29 Y. Zhang and P. S. Cremer, *Curr. Opin. Chem. Biol.*, 2006, **10**, 658–663.
30 H. Oki, Y. Matsuura, H. Komatsu and A. A. Chernov, *Acta Cryst. D*, 1999, **55**, 114–121.
31 J. Grigsby, H. Blanch and J. Prausnitz, *Biophys. Chem.*, 2001, **91**, 231–243.
32 F. Zhang, G. Zocher, A. Sauter, T. Stehle and F. Schreiber, *J. Appl. Cryst.*, 2011, **44**, 755–762.
33 A. Salis, F. Cugia, D. F. Parsons, B. W. Ninham and M. Monduzzi, *Phys. Chem. Chem. Phys.*, 2012, **14**, 4343–4346.
34 S. Abe, B. Maity and T. Ueno, *Curr. Opin. Chem. Biol.*, 2018, **43**, 68–76.
35 J.-P. Guilloteau, M. M. Ries-Kautt and A. F. Ducruix, *J. Cryst. Growth*, 1992, **122**, 223–230.
36 M. C. Vaney, I. Broutin, P. Retailleau, A. Douangamath, S. Lafont, C. Hamiaux, T. Prangé, A. Ducruix and M. Riès-Kautt, *Acta Cryst. D*, 2001, **57**, 929–940.
37 H. Sedgwick, K. Kroy, A. Salonen, M. B. Robertson, S. U. Egelhaaf and W. C. K. Poon, *Eur. Phys. J. E: Soft Matter Biol. Phys.*, 2005, **16**, 77–80.
38 J. Hansen, R. Uthayakumar, J. S. Pedersen, S. U. Egelhaaf and F. Platten, *Phys. Chem. Chem. Phys.*, 2021, **23**, 22384–22394.
39 L. Hentschel, J. Hansen, S. U. Egelhaaf and F. Platten, *Phys. Chem. Chem. Phys.*, 2021, **23**, 2686–2696.
40 M. Madani, T. Hamacher and F. Platten, *Soft. Matter.*, 2025, **21**, 1937–1948.
41 F. Zhang, M. K. Feustel, M. W. Skoda, R. M. Jacobs, F. Roosen-Runge, T. Seydel, M. Sztucki and F. Schreiber, *Phys. A*, 2024, **650**, 129995.
42 O. Matsarskaia, F. Roosen-Runge and F. Schreiber, *Chem. Phys. Chem.*, 2020, **21**, 1742–1767.
43 S. Alberti and A. A. Hyman, *Nat. Rev. Mol. Cell Biol.*, 2021, **22**, 196–213.
44 T. P. J. Knowles, M. Vendruscolo and C. M. Dobson, *Nat. Rev. Mol. Cell Biol.*, 2014, **15**, 384–396.
45 C. J. Roberts, *Curr. Opin. Biotechnol*, 2014, **30**, 211–217.
46 R. Mezzenga and P. Fischer, *Rep. Prog. Phys.*, 2013, **76**, 046601.
47 T. P. J. Knowles and R. Mezzenga, *Adv. Mater.*, 2016, **28**, 6546–6561.
48 M. Taleb, C. Didierjean, C. Jelsch, J. Mangeot, B. Capelle and A. Aubry, *J. Cryst. Growth*, 1999, **200**, 575–582.
49 D. Hou and H.-C. Chang, *Appl. Phys. Lett.*, 2008, **92**, 223902.
50 H. Koizumi, K. Fujiwara and S. Uda, *Cryst. Growth Des.*, 2009, **9**, 2420–2424.
51 H. Koizumi, S. Uda, K. Fujiwara and J. Nozawa, *J. Cryst. Growth*, 2010, **312**, 3503–3508.
52 H. Koizumi, S. Uda, K. Fujiwara, M. Tachibana, K. Kojima and J. Nozawa, *J. Appl. Cryst.*, 2013, **46**, 25–29.
53 A. Rodríguez-Romero, N. Esturau-Escofet, C. Pareja-Rivera and A. Moreno, *Crystals*, 2017, **7**, 179.
54 C. N. Nanev, *Crystals*, 2017, **7**, 310.
55 C. Pareja-Rivera, M. Cuéllar-Cruz, N. Esturau-Escofet, N. Demitri, M. Polentarutti, V. Stojanoff and A. Moreno, *Cryst. Growth Des.*, 2017, **17**, 135–145.

56 M. Taleb, C. Didierjean, C. Jelsch, J. Mangeot and A. Aubry, *J. Cryst. Growth*, 2001, **232**, 250–255.
57 Z. Hammadi, J.-P. Astier, R. Morin and S. Veesler, *Cryst. Growth Des.*, 2007, **7**, 1472–1475.
58 H. Koizumi, K. Fujiwara and S. Uda, *Cryst. Growth Des.*, 2010, **10**, 2591–2595.
59 C. N. Nanev and A. Penkova, *J. Cryst. Growth*, 2001, **232**, 285–293.
60 D. Ray, M. Madani, J. K. G. Dhont, F. Platten and K. Kang, *J. Phys. Chem. Lett.*, 2024, **15**, 8108–8113.
61 M. Shah, O. Galkin and P. G. Vekilov, *J. Phys. Chem. B*, 2009, **113**, 7340–7346.
62 F. Platten, J. Hansen, J. Milius, D. Wagner and S. U. Egelhaaf, *J. Phys. Chem. B*, 2015, **119**, 14986–14993.
63 K. Kang and F. Platten, *Sci. Rep.*, 2022, **12**, 3061.
64 K. Kang and J. K. G. Dhont, *Soft Matter*, 2010, **6**, 273–286.
65 P. S. Mohanty, S. Nöjd, M. J. Bergman, G. Nägele, S. Arrese-Igor, A. Alegria, R. Roa, P. Schurtenberger and J. K. G. Dhont, *Soft Matter*, 2016, **12**, 9705–9727.
66 G. J. Janz, B. G. Oliver, G. R. Lakshminarayanan and G. E. Mayer, *J. Phys. Chem.*, 1970, **74**, 1285–1289.
67 S. Mohanakumar and S. Wiegand, *Eur. Phys. J. E: Soft Matter Biol. Phys.*, 2022, **45**, 10.
68 M. Ataka and M. Asai, *J. Cryst. Growth*, 1988, **90**, 86–93.
69 P. A. Darcy and J. M. Wiencek, *J. Cryst. Growth*, 1999, **196**, 243–249.
70 V. Bhamidi, E. Skrzypczak-Jankun and C. Schall, *J. Cryst. Growth*, 2001, **232**, 77–85.
71 X. H. Tang, J. J. Liu, Y. Zhang and X. Z. Wang, *J. Cryst. Growth*, 2018, **498**, 186–196.
72 P. S. Chow, X. Y. Liu, J. Zhang and R. B. H. Tan, *Appl. Phys. Lett.*, 2002, **81**, 1975–1977.
73 J. Hansen, S. U. Egelhaaf and F. Platten, *Phys. Chem. Chem. Phys.*, 2023, **25**, 3031–3041.
74 J. K. G. Dhont, *An Introduction to Dynamics of Colloids*, Elsevier, 1996.
75 P. R. ten Wolde and D. Frenkel, *Science*, 1997, **277**, 1975–1978.
76 P. R. ten Wolde and D. Frenkel, *Theor. Chem. Acc.*, 1999, **101**, 205–208.
77 R. J. Yang, S. Q. Li and Q. H. Zhang, *J. Food Sci.*, 2004, **69**, FCT241.
78 W. Zhao and R. Yang, *Food Chem.*, 2008, **110**, 334–343.
79 G. Urabe, T. Katagiri and S. Katsuki, *Bioelectricity*, 2020, **2**, 33–39.
80 A. Stradner, H. Sedgwick, F. Cardinaux, W. C. K. Poon, S. U. Egelhaaf and P. Schurtenberger, *Nature*, 2004, **432**, 492–495.
81 Y. Liu, L. Porcar, J. Chen, W.-R. Chen, P. Falus, A. Faraone, E. Fratini, K. Hong and P. Baglioni, *J. Phys. Chem. B*, 2011, **115**, 7238–7247.
82 R. A. Curtis, J. M. Prausnitz and H. W. Blanch, *Biotechnol. Bioeng.*, 1998, **57**, 11–21.
83 Y. Zhang and P. S. Cremer, *Proc. Nat. Acad. Sci. U. S. A.*, 2009, **106**, 15249–15253.
84 J. Hansen, J. N. Pedersen, J. S. Pedersen, S. U. Egelhaaf and F. Platten, *J. Chem. Phys.*, 2022, **156**, 244903.
85 P. Holmqvist, M. P. Lettinga, J. Buitenhuis and J. K. G. Dhont, *Langmuir*, 2005, **21**, 10976–10982.
86 F. Mura and A. Zaccone, *Phys. Rev. E*, 2016, **93**, 042803.
87 D. Tanaka, R. Hijiya and T. Wakamatsu, *J. Cryst. Growth*, 2021, **573**, 126288.
88 S. Takashima and K. Asami, *Biopolymers*, 1993, **33**, 59–68.
89 J. K. G. Dhont and K. Kang, *Eur. Phys. J. E: Soft Matter Biol. Phys.*, 2010, **33**, 51–68.
90 J. Zhou and F. Schmid, *Eur. Phys. J. E: Soft Matter Biol. Phys.*, 2013, **36**, 33.